SiC-Based Resonant Converters With ZVS Operated in MHz Range Driving Rapidly Variable Loads: Inductively Coupled Plasmas as a Case of Study

Santiago Eizaguirre Cabrera, Tim Gehring, Fabian Denk, Qihao Jin, Jan Dycke, Manuel Renschler, Marc Hiller, *Member, IEEE*, Uli Lemmer, *Member, IEEE*, and Rainer Kling, *Member, IEEE*

***Abstract*—Wide band-gap resonant converters operating with zero voltage switching (ZVS) recently proved the conversion of up to 25 kW at 3 MHz with an efficiency of ≈94%. This is of special interest for any application where power in middle frequency range is required since typically achieved efficiencies for those frequencies are in the range of 60%–70%. Inductively coupled plasma (ICP) based applications would significantly benefit from this fact, but they entail special driving challenges. ICP loads exhibit strong impedance variations during ignition and operation, which means a high limitation factor when driving them with resonant converters. This article offers a deeper look into this topic through the example of a 10 Pa Xenon lamp. The ignition transient is measured and analyzed while driving the system with a Silicon Carbide (SiC)-based resonant converter. An FEM simulation modeling the electromagnetic, thermal, mechanical, and plasma properties is also performed. The results are contrasted with the corresponding measurements showing as well the simulation usefulness as a design tool. Theoretical calculations of the intrinsic limits for ZVS resonant power conversion are also offered. This provides an insight into which analysis and control methods would make ICP loads compatible with these converters and, therefore, able to benefit completely from their efficiency and power density benefits.**

***Index Terms*—Inductive coupled plasma (ICP), MHz resonant converters, plasma impedance, SiC power MOSFETs, zero voltage switching (ZVS).**

I. Introduction

RESONANT converters promise high efficiencies and power densities for dc–ac power conversion, even at power levels over 10 kW and at frequencies in MHz range. However, their success is strongly dependent on the load to be driven. For loads for which the impedance remains constant, the converter design is straightforward [1]. In contrast, loads that show an impedance variation during operation could lead not only to an improper and not optimal operation but also to the complete converter destruction. This makes the design in many cases especially difficult if not impossible. Unsolvable design issues prohibit several applications in which the load impedance varies in magnitude and/or phase from being able to fully profit from resonant converters benefits. This is mainly because the operation in MHz frequency range is only possible by reducing the switching losses dramatically, which is done by means of zero voltage switching (ZVS). But to enable ZVS, certain conditions on load current amplitude and phase shift must be satisfied. If these requirements are not met, the transistors would immediately operate with hard-switching, which at MHz range means enough thermal power at the die to destroy the transistors after a couple of switching cycles.

Inductively coupled plasma (ICP) loads cover a wide variety of applications, which are currently in high demand by the industry [2]. The semiconductor industry, surface treatment processes, nanoparticle synthesis, waste treatment, and high power UV radiation sources are examples of applications that would substantially benefit from resonant converters [3]–[9]. The power sources that are currently used in those fields, which are mostly linear amplifiers, have efficiencies around 60%, leading to not only high energy losses but also the need for high cooling efforts and large converter volumes. Resonant converters with ZVS are able to achieve efficiencies over 90% for powers over 10 kW and at frequencies in MHz range [10]–[14]. This fact could enable an enormous change in the mentioned industry fields. However, the problem of the load sensitivity must be addressed and solved first.

The electrical impedance of an ICP can be derived by modeling the system as a transformer, where the primary side corresponds to the used coil, and the secondary to the plasma volume modeled as a single-turn winding [2], [15], [16]. The finite plasma conductivity determines the resistive component seen at the primary side. The inductive component is determined by the geometry of the conductive plasma region, as well as the inertia of the charged particles in the plasma. However, the influence of this latter has usually a negligible effect in comparison with the geometry associated [2].

Manuscript received July 19, 2021; revised October 28, 2021 and December 28, 2021; accepted January 22, 2022. Date of publication February 1, 2022; date of current version March 24, 2022. Recommended for publication by Associate Editor M. Ponce-Silva. *(Corresponding Author: Santiago Eizaguirre Cabrera.)*

Santiago Eizaguirre Cabrera, Tim Gehring, Fabian Denk, Qihao Jin, Jan Dycke, Marc Hiller, Uli Lemmer, and Rainer Kling are with the Light Technology Institute, Karlsruhe Institute of Technology, l76137 Karlsruhe, Germany (e-mail: santiago.eizaguirre@kit.edu; tim.gehring@kit.edu; fabian.denk@kit.edu; qihao.jin@kit.edu; jan.dycke@kit.edu; marc.hiller@kit.edu; uli.lemmer@kit.edu; rainer.kling@kit.edu).

Manuel Renschler is with the University of Applied Sciences, 76133 Karlsruhe, Germany (e-mail: rema1082@h-ka.de).

Color versions of one or more figures in this article are available at https://doi.org/10.1109/TPEL.2022.3147947.

Digital Object Identifier 10.1109/TPEL.2022.3147947

ICP loads show different impedance variations which make it especially challenging when driving them with resonant converters [16], [17]. First, the ignition transient takes place, which is typically the fastest and greatest impedance change. This change is associated with the transition from electrostatic-to-electromagnetic mode [19]–[23] and the consequent plasma expansion in the vessel volume. After ignition, one may need to deal with impedance changes of different nature, depending on the application. All of them occur with time constants much greater than that which are associated with plasma expansion. In low- to high-pressure plasmas, such as plasma torches or special light sources, a thermal transient is present, within which the temperature increases, changing the plasma conductivity [2], the charge carriers' distribution and, through this, the impedance seen at the driving coil. Applications where specific materials are injected into the plasma [4], [6], [8] to induce a certain reaction, also show an impedance change during the injection. Furthermore, for all pressures levels, ICP loads show a significant impedance variation with the coupled power and the driving frequency. Finally, certain light sources which have a biphase filling at room temperature exhibit a strong impedance transient during the evaporation of the nongas phase material.

A. Objective Definition and Work Structure

This work aims to gain more insight into the impedance variations that ICP loads exhibit and the possible ways to handle them when driving such loads with resonant converters. It is a step toward higher efficiency converters in MHz frequencies which are able to drive generic ICP loads, providing knowledge and tools for designing such a system for a certain given application.

A representative and simple example, a Xenon low pressure lamp, is analyzed. Despite the relatively low power at which the lamp was driven and the fact that not every mentioned impedance change takes place here, this lamp has the same qualitative behavior of almost all other ICP load types. The ignition transient in particular can be observed in detail, which is the fastest and the one that normally leads to converter destruction.

The lamp was driven in open loop with a Silicon Carbide (SiC)-based resonant converter. The coil impedance was measured before, during, and after plasma ignition.

Moreover, an FEM simulation model of the lamp was implemented. This gives even more insight into the phenomena which take place in the load under study, allowing the analysis of physical nonmeasurable quantities inside the lamp. It also allows for an impact evaluation of design variables' changes, such as coil geometry, filling pressure, among others, which is normally extremely time-consuming to carry out experimentally.

Starting from the converter point of view, a brief description of its working principle, the necessity of ZVS, and its requirements are given in Section II. Section III presents the implementation of the simulation. The measurement setup description follows in Section IV. The actual measurement and simulation results are shown and compared in Section V, followed by their extended analysis in Section VI, where a general control scheme is presented. Finally, Section VII concludes this article.

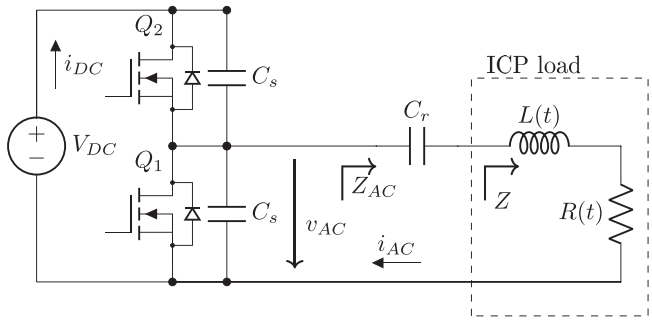

Fig. 1. Schematic of the system under study: Half-bridge inverter with a series resonant load, composed of a series resonant capacitor, and the ICP load.

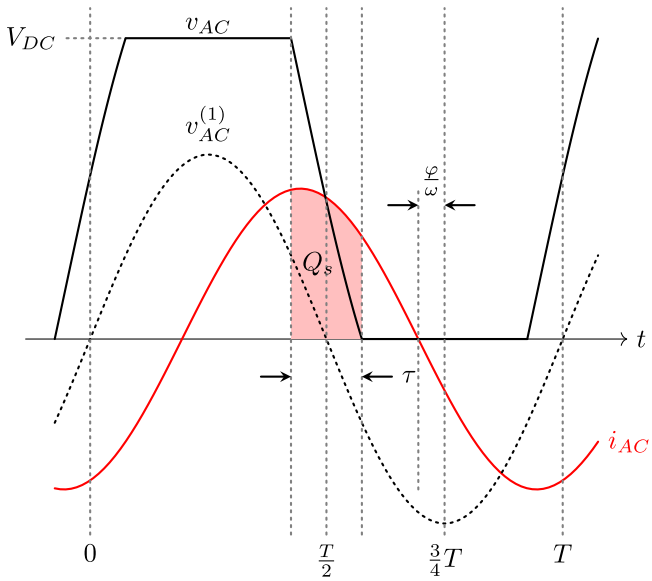

Fig. 2. Typical voltage and current waveforms of a half-bridge operating with ZVS. Example with $|Z_{\rm AC}| = \frac{98\times10^{-3}}{C_s f}$ and $\varphi = 20^o$. The dashed black curve corresponds to the first harmonic of the inverter output voltage $v_{\rm AC}$.

II. Resonant Converters With Zero Voltage Switching

The simplest form of the system under study is shown in the schematic of Fig. 1, and the respective waveforms in Fig. 2. In this case, the resonant circuit is just composed of a series *RLC*-circuit as the simplest example. More complex networks are also used, being the whole content of the present work also applicable in those cases. This simplicity of the series *RLC*-circuit gives the advantage of having fewer components, which in many cases imply higher power density and efficiency, but in some applications a more complex resonant circuit might be needed to achieve the required impedance transformation [24]–[26].

The output current $i_{\rm AC}$ must be positive when the high side transistor Q_2 turns OFF, which implies the necessity of an inductive component, i.e., $\mathrm{Im}(Z_{\rm AC}) > 0$. In addition, the current must be high enough so that, with the used snubber capacitance C_s, the charge Q_s can be taken out by $i_{\rm AC}$, and the output voltage can commutate before the current changes its polarity. In a real case, C_s includes the effective output capacitance of the used

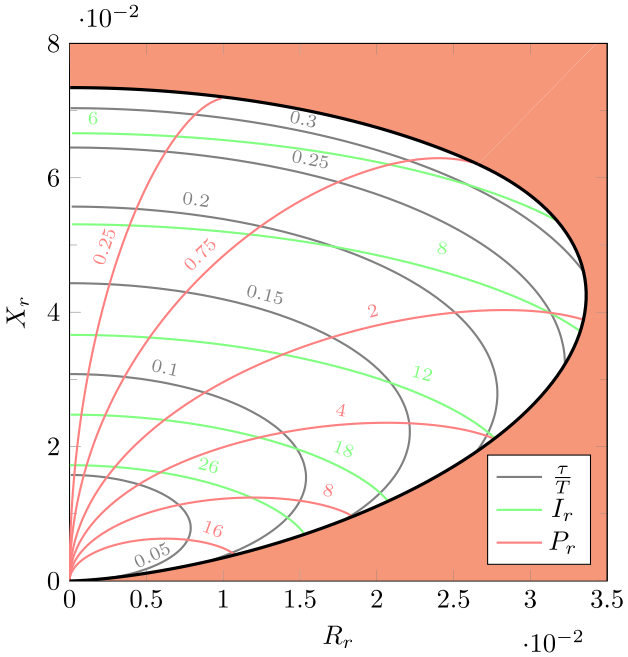

Fig. 3. Safe operation area (SOA) of a generic ZVS resonant half-bridge in the resistance–reactance plane where the axes are the normalized quantities $R_r = RC_s f$ and $X_r = XC_s f$.

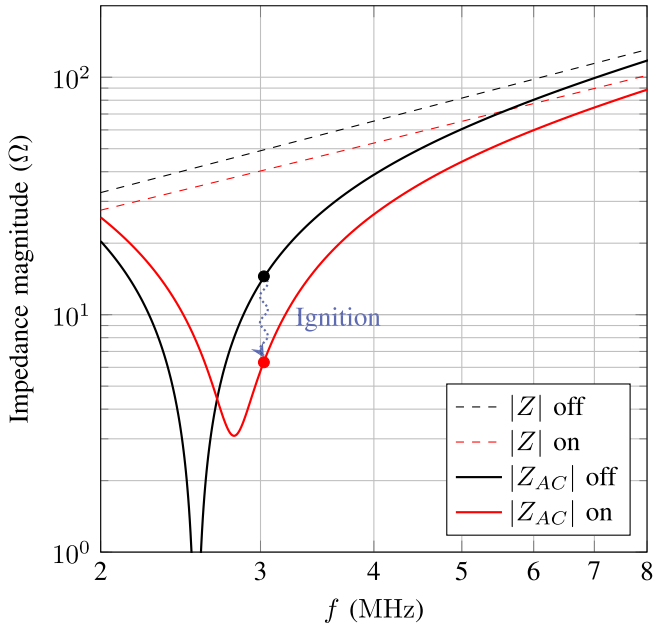

Fig. 4. Example load impedance Z, and impedance seen at the inverter output Z_{AC} on the frequency domain, in ON- and OFF-state.

transistors as well. These conditions relate the impedance Z_{AC} with the operating frequency f and snubber capacitance C_s, determining the allowed region for Z_{AC}. Writing the impedance seen at the half-bridge output as $Z_{\mathrm{AC}} = R + jX$, and normalizing it by the value $1/C_s f$, it is possible to describe the impedance region where ZVS is achieved, as shown in Fig. 3. The reactive component X determines the current component[1] in quadrature with the voltage first harmonic, and is responsible for achieving ZVS. The diagram of Fig. 3 applies for every half-bridge, is neither dependent on the dc voltage V_{DC} nor on the connected circuit at the output, but just on the characteristic quantity $C_s f$. In the colored regions ZVS is not achieved. Especially remarkable is the fact that for every point in the allowed region, the output voltage waveform (characterized by the switching time ratio τ/T), the normalized output current $I_r := \frac{I_{\mathrm{AC}}}{V_{DC} C_s f}$, and the normalized transferred active power $P_r := \frac{P}{V_{DC}^2 C_s f}$ are defined. Contour lines of these three quantities are also shown in Fig. 3. A more detailed explanation of this diagram is given in Appendix A.

For a constant load with a fixed inductive and resistive component, the system design is reduced to the task of finding values for C_s and f, and the appropriate load impedance transformation (a simple series capacitor or a combination of reactive components with transformers) so that the operating point lies in the allowed region. The system can then be operated and controlled easily and without risks, determining the desired power transfer by means of just the dc voltage. The case of ICPs is although not that straightforward. Their reactive and resistive parts change during operation, and these changes can easily push the operating point of the inverter out of the presented allowed region.

As an example, the plasma ignition process represents one of the greatest and fastest impedance changes. In OFF state, the inverter will operate somewhere in the allowed region at the vertical axis ($R_r = 0$). Seen in frequency domain, the initial point will be over the resonance frequency (black curve and point in Fig. 4), close enough to the resonance frequency so that the needed current for ignition can be achieved. When plasma expansion starts, the equivalent coil series inductance decreases (which makes the resonant frequency increase) and the equivalent resistance increases. Hence, the impedance over frequency after ignition will resemble the red curve in Fig. 4. If the switching frequency is kept constant, the new operating point will be the red dot. If the initial point was too close to the resonant frequency, the final operating point could be on the capacitive side (left from resonant frequency), where ZVS is lost. This is likely to happen in applications where high magnetic fields are required for ignition. Not only the fact of being capacitive or inductive is what matters but, because of the resistance which is now present in the circuit, one should address the problem with the perspective of the diagram from Fig. 3. Both the end operating point and the path that Z_{AC} takes during ignition (but also because of any other change in the system) should be in the allowed region. To analyze, measure, and simulate this path is the focus of the present work.

III. Simulation

The simulation was performed with the finite element software COMSOL Multiphysics (COMSOL AB, Stockholm, Sweden) [27]. The heat transfer, Maxwell, fluid dynamics, and plasma physics equations are solved by different modules which

[1]For the case under study, it summarizes the inductive component of the ICP, and the capacitive component of the series–resonant capacitor.

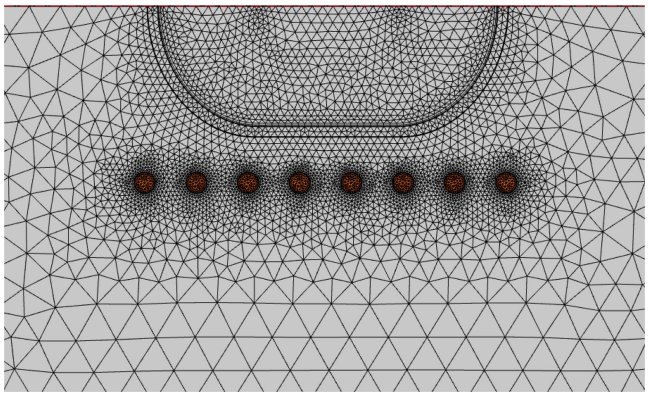

Fig. 5. Main part of the simulated mesh with 8710 elements. The extern air region extends 20 cm width and 10 cm height, and the lamp body is 7 cm long.

interact with each other, coupled through the physical magnitudes they share.

The coil excitation is determined by an additional module that allows the definition of a lumped element circuit through a netlist. A constant ac voltage source (representing $v_{\mathrm{AC}}^{(1)}$) and the resonant capacitor were connected in this circuit in series with a port element that represents the coil. This allows a coupling between a linear circuit of lumped elements (the ac source and the series capacitor) with a simulation of coil and lamp where the physics of the system are modeled and solved. In the physical model, voltage and current of the coil are calculated for every time step. This values summarize the behavior of the system as a passive component, allowing its addition as a lumped-port element in the linear circuit.

The simulation was implemented under a 2-D axis revolution symmetry. The mesh used is depicted in Fig. 5.

A. Plasma Module

Of particular importance for the present work is the module which models the plasma physics, and therefore will be presented briefly here. This module solves the following [28]:

$$\frac{\partial n_e}{\partial t} + \vec{\nabla}\cdot\vec{\Gamma}_e = R_e - (\vec{u}\cdot\vec{\nabla})n_e \tag{1}$$

$$\vec{\Gamma_e} = -(\mu_e\vec{E})n_e - \vec{\nabla}(D_e n_e)$$

$$\frac{\partial n_\varepsilon}{\partial t} + \vec{\nabla}\cdot\vec{\Gamma_\varepsilon} + \vec{E}\cdot\vec{\Gamma_e} = S_{en} - (\vec{u}\cdot\vec{\nabla})n_\varepsilon + \frac{Q+Q_{\mathrm{gen}}}{q}$$

$$\vec{\Gamma_\varepsilon} = -(\mu_\varepsilon\vec{E})n_\varepsilon - \vec{\nabla}(D_\varepsilon n_\varepsilon). \tag{2}$$

With (1), the time-dependent change of the electron density n_e is calculated. Here, μ_e denotes the electron mobility, $\vec{E}$ the electric field, D_e the diffusion coefficient, and $\vec{u}$ represents the velocity vector of the neutral fluid (here Xenon) and is calculated by the laminar flow module of COMSOL Multiphysics. The rate of electron generation R_e is calculated by the usage of the collision cross sections for the different reactions and species. The cross-sectional data were imported to the software. Table I shows the used reactions for the presented simulation model with the data sources. The symbols n_ε, μ_ε, and D_ε in (2) are named analogously to (1) for the energy density. Q and Q_{gen} represent an external and a general heat source. In addition, q is the elementary charge and S_{en} indicates the energy change by inelastic collisions. For both equations, the flux terms $\vec{\Gamma_e}$ and $\vec{\Gamma_\varepsilon}$ are directly given.

TABLE I
USED PROCESSES IN THE XENON DISCHARGE FOR THE SIMULATION WITH THE DATA SOURCES

No.	Process	Reaction	$\Delta\varepsilon$ (eV)	Source
1	Elastic	$Xe + e \longrightarrow Xe + e$		[30]
2	Excitation	$Xe + e \longrightarrow Xe(6s_2) + e$	8.31	[31]
3	Excitation	$Xe + e \longrightarrow Xe(6s_1) + e$	8.43	[32]
4	Relaxation[1]	$Xe(6s_1) \longrightarrow Xe + h\nu$	-8.43	[33]
5	Ionization	$Xe + e \longrightarrow Xe^+ + 2e$	12.12	[34]
6	Step-Wise ionization	$Xe(6s_2) + e \longrightarrow Xe^+ + 2e$	3.44	[35]

It has to be noted that for a more compact nomenclature of the excited states the notation of Sommerer [29] was used.
[1]For this reaction the relaxation rate $2.73 \cdot 10^8\ s^{-1}$ was used.

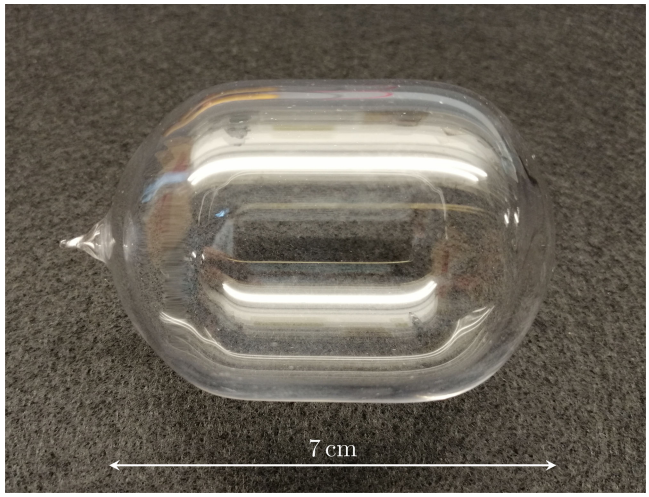

Fig. 6. Quartz lamp body filled with 10 Pa Xenon.

The electromagnetic field is calculated through Ampere's law, expressed as a function of the magnetic vector potential $\vec{A}$, given as

$$(j\omega\sigma - \omega^2\epsilon)\vec{A} + \vec{\nabla}\times(\mu_0^{-1}\vec{\nabla}\times\vec{A}) = \vec{J_e} \tag{3}$$

with the imaginary unit j, the permittivity ϵ, the vacuum permeability μ_0, and the external applied current density $\vec{J_e}$. The plasma conductivity σ is calculated by

$$\sigma = \frac{n_e q^2}{m_e(\nu_m + j\omega)} \tag{4}$$

where m_e represents the electron mass and ν_m the momentum transfer frequency, and ω the excitation frequency. A more detailed theory overview of the simulation method and the solved equations can be found in [28].

IV. SETUP DESCRIPTION

The lamp was filled with pure Xenon at 10 Pa. A picture of the quartz lamp body used can be seen in Fig. 6. The coil was

Fig. 7. Lamp in stabilized operation at 3.026 MHz and 150 W.

wound with 8 turns of $4\,\mathrm{mm}$ diameter copper tube. The total coil length was $70\,\mathrm{mm}$ and its radius $34\,\mathrm{mm}$.

The inverter is based on a SiC $1200\,\mathrm{V}$–$40\,\mathrm{m\Omega}$ half-bridge module, exposed in detail in [10] and [36]. It was driven at a constant frequency of $3.026\,\mathrm{MHz}$. The gate signals were separately generated and optically transferred. As snubber capacitors, $1.1\,\mathrm{nF}$ mica capacitors were used. A vacuum variable capacitor in the range of 50–1000 pF was used as the series resonant capacitor. The dc link was fed with the dc laboratory power supply EA-PS 91500-30 [37] (EA Elektro-Automatik GmbH & Co. KG, Germany).

The measurement setup was based on the oscilloscope MSO56 [38] (Tektronix GmbH, Germany), which for the measured transient was configured with a sample rate of 3.125 GS/s. For the load current, a Pearson current probe [39] was used, while for the dc current a hall effect probe [40]. The coil voltage, as well as the dc voltage, were measured with differential voltage probes [41] (PMK GmbH, Germany). An exhaustive deskew of the probes used at the coil was needed to have sufficient accuracy in the phase calculation. In order to capture the plasma ignition transient, a silicon optical detector [42] (DET10 A, Thorlabs Inc., USA) was used, which received the light of the lamp through a optical fiber whose end was placed close to the lamp. Its electrical output signal was used to trigger the oscilloscope.

V. Results

In this section, the measurements and simulation results are shown and compared. The measurements were performed in a time window of 20 ms, and the simulation of $650\,\mu\mathrm{s}$, because no significant changes were observed for longer times.

A. Measurements

With the lamp outside the coil, the resonance capacitance was adjusted to the value of $910\,\mathrm{pF}$ in order to ensure ZVS. Then, with the lamp inside the coil, the dc voltage was ramped up until the lamp ignition took place by $V_{DC} = 200\,\mathrm{V}$. In Fig. 7, the lamp in ON state is shown.

With the coil voltage and current measurement data, a cycle-by-cycle postprocessing was performed. For every switching period ($\sim 330\,\mathrm{ns}$), the first harmonic component of the coil current and voltage were calculated through their fast Fourier transform. Their respective amplitudes over time are shown in Fig. 8(a). Furthermore, the phase difference between these components was computed, determining lastly the coil complex impedance $Z = R + j\omega L$ and the coupled power. The resulting resistance and inductance are shown in Fig. 8(b). The mean value of the dc magnitudes associated with each switching cycle was calculated and can be seen in Fig. 8(c). After reaching steady-state operation a dc-to-ac efficiency of 93% was measured.

B. Simulation

The simulation was performed with a frequency transient analysis at $f = 3.026\,\mathrm{MHz}$, having a time step of $1\,\mu\mathrm{s}$.

The simulation results for the ignition transient at $303\,\mathrm{K}$ are exposed and compared with those measured in the same time scale in Figs. 9 and 10. This represents the dynamic impedance behavior. After this, the simulation was slightly changed and used to evaluate the static behavior, i.e., the dependence of the ON-state impedance with the operating frequency and coupled power.

1) Dynamic Behavior: In Figs. 9 and 10, the simulated and measured coil resistance and inductance, and coil current and voltage are shown, respectively, in a time scale of $650\,\mu\mathrm{s}$. The time $t = 0$ was set in both cases to the moment where the resistance reaches 2% of the final value.

Aiming to evaluate the impact of the gas filling pressure on the variables under analysis, the simulation was additionally run with a modification of $\pm 25\%$ of this pressure. The corresponding results for the resistance and inductance are depicted in Fig. 9.

2) Static Behavior: In this case, the coil excitation was not coupled with the defined netlist, but a fixed coupled power was set. This power and the frequency were used to implement a double parametric sweep and analyze the ON-state impedance variations in the range of 150–1200 W and 2–14 MHz, respectively. In Fig. 11, these results are shown in the resistance–inductance plane.

VI. Analysis and Discussion

A. 20 ms Measured Transient

In this time scale, the dynamics of two different phenomena are observable in the measurements. The first is associated with the plasma ignition, and the second is related to the internal control system of the dc power supply. The plasma expansion takes place between 40 and 200 μs in Fig. 8, producing the great impedance drop, which in turn makes the coil current increase. This is because this transient happens in a time-lapse considerably shorter than the reaction times of the dc power supply control system, making the inverter behave during this transient like a constant voltage power supply without current limit. For the presented measurements, the power supply was set with a current limit of 2 A. Simultaneously with the impedance drop is observed that the dc current rises rapidly, exceeding this limit. The reaction of the control system is observable at around

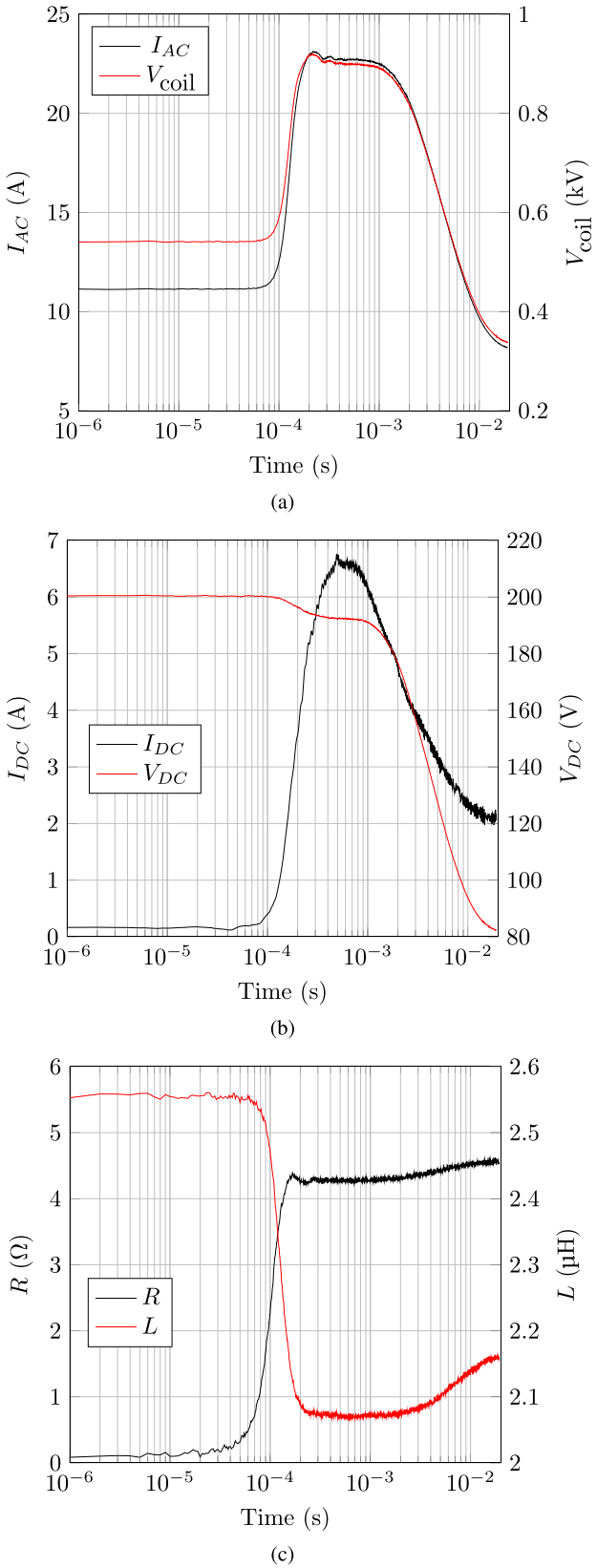

Fig. 8. Measured and derived quantities before, during, and after the E-H mode transition. (a) Coil current and voltage effective values. (b) DC current and voltage. (c) Coil resistance and inductance.

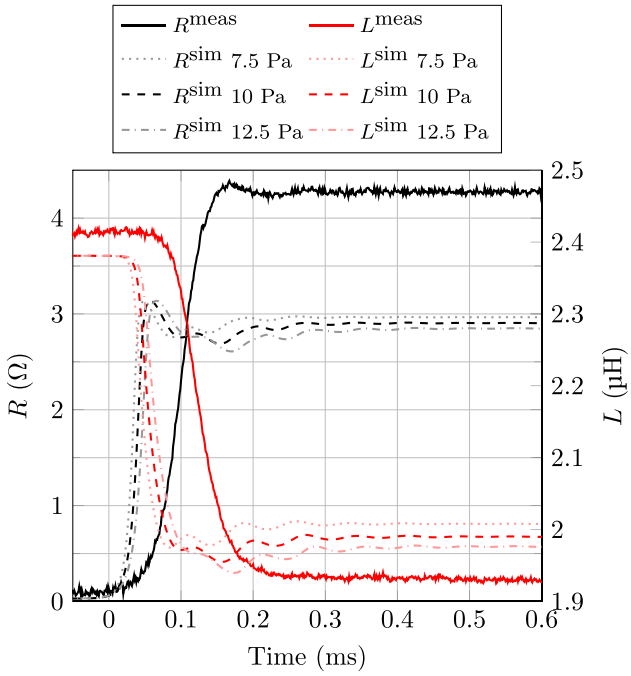

Fig. 9. Simulated and measured resistance and inductance during ignition. The light curves denote the impact of a ±25% variation on the filling pressure.

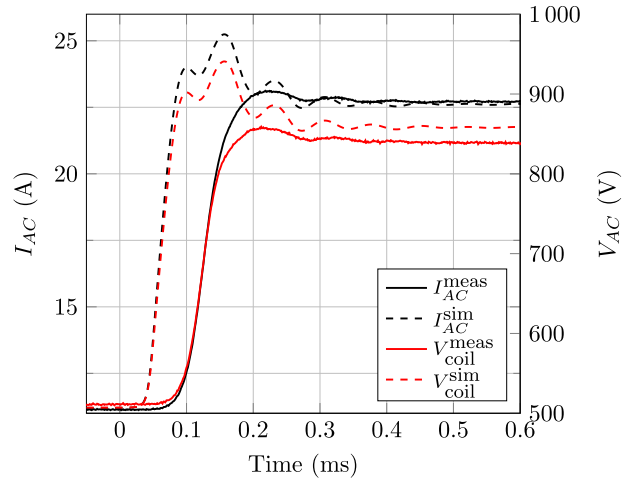

Fig. 10. Effective values of simulated and measured coil current and voltage during ignition.

400 μs. Until this point, a voltage drop in the dc voltage to 192 V is also noticeable. This can be attributed to the inductance of the dc-link cable, and the discharge of the dc film capacitors placed at the inverter board. From here on, the control system reduces the dc voltage, bringing also the dc (and consequently ac) current down to the programmed limit of 2 A. During this slow control transient, an increment of the inductance and resistance is observable in Fig. 8(c) for decreasing power. This is in accordance with the already predicted static behavior showed in Fig. 11.

The transient associated with the power supply control system is important to analyze, but it is strongly influenced by the rest

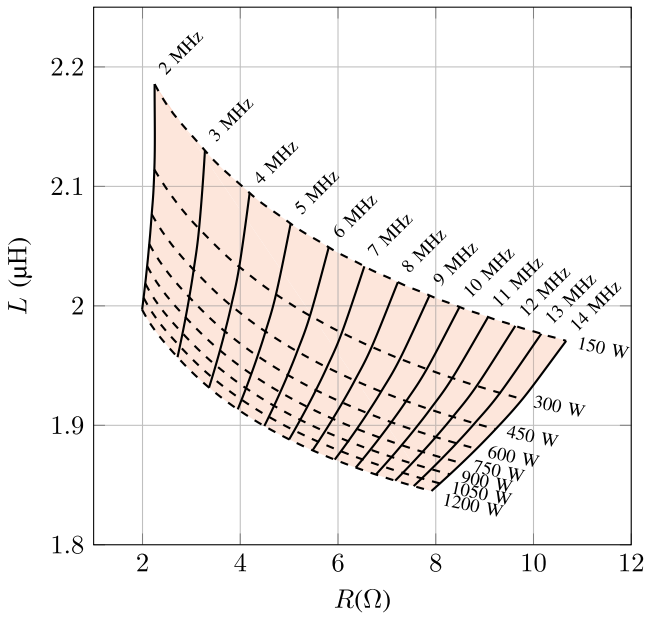

Fig. 11. Simulated impedance Z for the implemented coil, at constant coupled power (dashed lines), and constant excitation frequency (solid lines).

of the system, election of initial conditions, and possible control strategies applied on the whole system. For this work, its analysis serves just as a typical and valuable example. However, the characteristic and important transient is that of the plasma ignition. This will always take place and is completely independent from the rest of the system.

B. $650\,\mu$s *Transient*

In Figs. 9 and 10, a closer look at the ignition transient is taken. The corresponding inverter output waveforms at switching frequency time scale, are showed separately in Appendix B, where it can be seen that ZVS is actually achieved during the whole transient.

Observing the net variations in Figs. 9 and 10 that occur due to plasma ignition, the measured resistance variation is 50% greater than the simulated one. The measured inductance change is also 23% greater than the simulated. This is a reflection of a higher plasma conductivity in the simulation model. In a first instance, the effect of the filling pressure was evaluated because of the considerably high inaccuracy of the filling method. For this reason, the simulation was run with an altered pressure but, as it can be seen in Fig. 9, this was not enough to explain the discrepancy.

Two further possible signs of a lower plasma conductivity in the real system are also appreciable in Figs. 9 and 10. One is the slower rise time. The 10%–90% time for the resistance was $70\,\mu$s for the measured case, and $25\,\mu$s for the simulated case. The other is related to the oscillations observed immediately after the plasma expansion, both in the measured and simulated magnitudes. The clearly higher damping factor in the measured case is in accordance with a higher plasma resistivity. These oscillations are produced by the excitation of electromechanical waves that resonate with the lamp body mechanical normal modes, caused by the pressure gradient during the ignition [43], [44]. Their analysis is not only uninteresting for the present work but it would also exceed its scope.

All these indicators of a higher plasma resistivity in the measured system suggest the absence of reactions in the simulation model [19]. It is known that considerably more reactions than the five shown in Table I take place in reality [45]. These five are just the most dominant ones. However, the complexity of an exhaustive description of all reactions rises up rapidly, especially for other gases. Not only to find the coefficients for each reaction but also the computing effort increases dramatically. On this point, it should be decided for each case if it is possible and worth expanding the simulated reactions set. This work shows that with just those five reactions, the simulated ignition transient has the same qualitative behavior as the measurements. The simulated time constant of the ignition dynamic was in the same order of magnitude and lower than the measured one. This makes the simulation a useful and conservative case when using it for the design of a control system. The computing time was within $20\,\mathrm{min}$ for a standard office computer, making the simulation a useful design tool.

To evaluate the temperature impact on the impedance variations, the simulation was run additionally for temperatures of $0\,^{\circ}\mathrm{C}$ and $600\,^{\circ}\mathrm{C}$. Since the lamp is a closed system, the starting pressure was changed to the corresponding values of 9 and $28.8\,\mathrm{Pa}$, respectively. This results from the modeling as ideal gas. The impedance in ON-state within this temperature range did not show variations greater than $1.9\,\%$. The dynamic of the ignition, i.e., the transition time, showed even smaller variations. This result is of special value, since it means, the dynamic under study is almost temperature independent, simplifying considerably the design of a control system. Experimentally, it is not straightforward to determine the dynamic differences just due to the temperature since other stronger effects are superposed, namely the current at which ignition occurs. This variable is strongly temperature dependent, but also dependent on the lamp history (when, how long and at which power it was driven for the last time). A detailed study of this behavior exceeds the scope of the present work, and deserve a separate analysis.

A last noticeable difference is in the OFF-state value of inductance. This is naturally not related to plasma properties and could be explained by the simplification of the simulated system by making it axis-symmetric. The total enclosed magnetic flux in the real helical coil is $30\,\mathrm{nH}$ higher than the simple addition of separate rings. Moreover, the field distribution is not exactly the same in both cases.

C. Ignition Impedance Path, ZVS, and Possible Control Methods

The previously presented results can be also analyzed in the resistance–reactance plane. In Fig. 12, the light red curve shows the measured path that the coil impedance Z takes during ignition, from the OFF-state at point A to the full plasma expansion at point B. The already described transient caused by the slow reaction of the power supply corresponds to the path B–C.

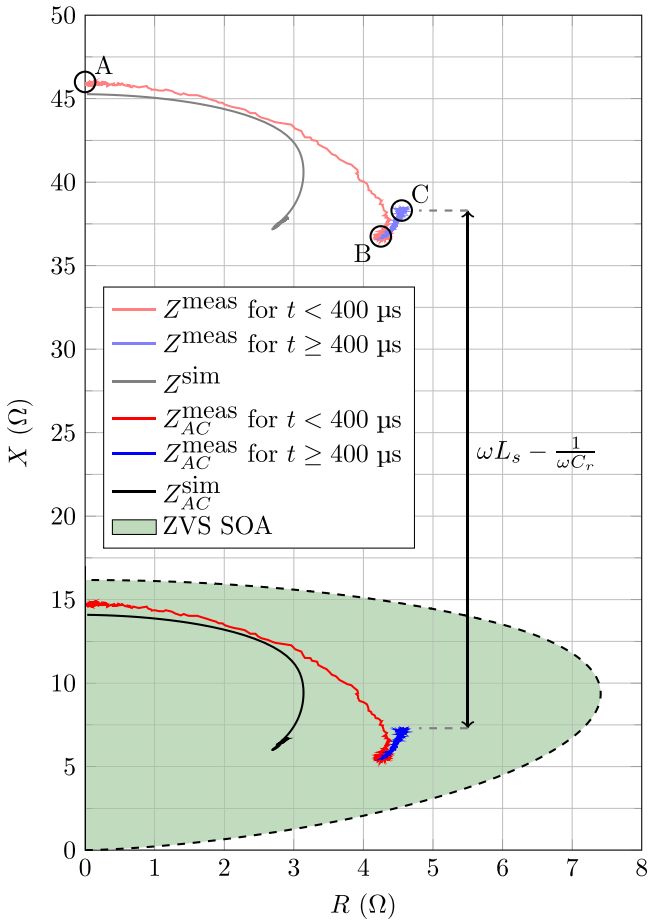

Fig. 12. Impedance path during ignition. Point A corresponds to the OFF-state, B to the end of plasma expansion, and C after the dc power supply controlled the dc current back to its set value.

The corresponding simulation results (which just describes the ignition) are plotted in gray.

From a general perspective, the impedance Z will be transformed by a certain network to the impedance seen at the inverter output. In the present study, this transformation is just a series capacitor, which means a subtraction in the reactive component by the value $1/\omega C_r$. Graphically, it is no more than a shift of the whole path in the vertical direction. Additionally, the series stray inductance L_s in the setup cabling that connects the inverter, the capacitor, and the coil, is not neglectable and must be considered. This has the opposite effect as the capacitor, producing an addition on the reactive component of ωL_s. For the used setup, it was measured, resulting in $L_s = 1.4\,\mu$H. The impedance transformation for more complex networks has usually not such an easy geometrical interpretation. In those cases, the analysis with Smith charts provides a simple interpretation of the transformation.

In any case, the impedance transformation must assure that the impedance seen by the inverter (Z_{AC}) lays in its SOA where ZVS is achieved, before, during, and after ignition. In Fig. 12, the green area indicates this SOA, the same presented in Section II and shown in Fig. 3. It corresponds to a snubber capacitance of $C_s = 1.5\,$nF, value measured directly on the inverter board. Reasons for being greater than the $1.1\,$nF used capacitors are mainly the addition of the effective output capacitance C_{oss} of the transistors, manufacturing deviation of the capacitors, and layout parasitics.

In Fig. 12, it can be clearly seen that the used transformation was successful and during the whole transient Z_{AC} moves in the green area, and therefore ZVS is always achieved. Otherwise, all measurements would have not been feasible. Many other cases may not be as straightforward and easy as the showed one. For assuring the impedance path into the SOA, one may consider different design and control freedom degrees. The coil geometry and number of turns definition sets the variation room for Z. The definition of the SOA is basically just made by the snubber capacitance C_s (given a desired frequency f, which is normally the case), but several practical restrictions may be considered as follows.

1) The desired C_s must be feasible to solder without introducing big stray inductances in the commutation loop. Otherwise, each switching event will produce high voltage overshoot and oscillations that could lead to ZVS loss.
2) The desired C_s may not be too small: at certain C_s values, when it is comparable with C_{oss} of the used transistors, the switching losses are not neglectable any more, being rapidly a thermal limitation [46].
3) Even if the switching losses are not a problem, too small values of C_s could lead to too high dV/dt during commutation, producing eventually problematic electromagnetic interference.
4) The used gate drive system has always a finite accuracy for defining the switching events, which carries to the need of leaving the corresponding safety margins to the SOA borders.

The last four points mean just restrictions on the available region in the SOA.

An important remaining design freedom degree is the impedance transformation. Multiple designs are possible, being this task a well-known and already investigated area [26]. The starting impedance region (definition of the lamp and coil) must be well defined, as well as the desired end impedance region (SOA), what makes this design stage the linking one between the other two.

Regarding possible control methods for such a system, there are at least three variables that can practically be modified as follows:

1) the dc voltage V_{DC};
2) impedance transformation parameters: typically mechanical variations of variable capacitors in the used network;
3) the switching frequency f.

The first one affects the system in just one dimension, the power. It does not affect the operating point in the normalized SOA region. Just side effects could occur for this case, like the cause of an impedance change due to the power dependence of the load. The second one could offer control freedom degrees for compensating changes in the load. However, its mechanical nature makes it so slow that just the slowest (thermal and evaporation) transients can be compensated with this method. It could also be used for moving the system to another desired operating

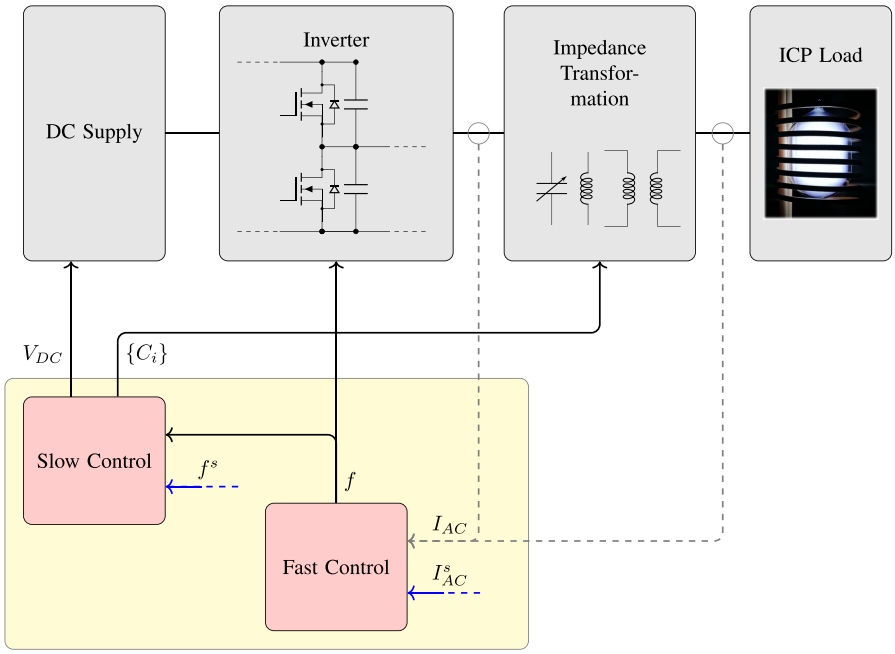

Fig. 13. Proposed general control scheme. Impedance changes associated to plasma ignition are compensated by a fast frequency change. Other slower variations in the system can be counteracted through the adjustment of the impedance transformation and the dc supply set points.

point since for this task it is not required to be fast. The last one, the switching frequency, offers the fastest reaction times, making it the only suitable way to compensate the ignition transient. The impact that a frequency variation during ignition could have, depends on the used impedance transformation network. For the presented case of a series capacitor, it is for example not possible to affect the resistive component through this but just the reactive one. Other networks, for example with a parallel capacitor to the load, could make also possible a variation of the resistive component through the frequency. Another advantage of varying the frequency during ignition is that more ICP loads could be driven, loads that otherwise (with a constant frequency) are either not able to ignite or ZVS will be lost after ignition. This is because for those loads that need an especially high magnetic field (and therefore high current) for the ignition, it is needed to operate the system before ignition closer to the resonant frequency (in Fig. 12 means shifting the initial point of the curve down toward zero). In these conditions, the impact of the load inductance reduction could imply either to take the system out of the SOA or, if not, to have too high currents for the used transistors. Both problems could be avoided through a simultaneous change of the frequency. Such a frequency variation could be made for example to held the magnitude of the impedance Z_{AC} constant during ignition, and therefore, also the magnitude of the current.

In summary, a general control scheme of an arbitrary system should be like the one shown in Fig. 13. A fast control unit will observe the currents on the ac side and consequently act on the switching frequency for compensating fast variations. If after a fast variation (for example plasma ignition) the switching frequency is not the desired one (f^s), slow changes on the matching network can be done to shift the operating point, and so the frequency back. The fast control system will follow this shift keeping the current constant. The control of the power can still be done via the dc voltage, with the time constant of the power supply.

VII. Conclusion

This article provides, through a simple example, a deep insight into the challenge of driving arbitrary ICP loads with resonant converters. It shows its measured and simulated impedance behavior, demonstrating as well that the simulation is a useful prediction and design tool. This work contributes to understand the dynamic behavior of an ICP load, showing and giving the tools for designing a control system for resonant converters with ZVS. This would enable to exploit the high efficiencies of such converters in a vast field of applications where rapidly changing loads demand several kW at MHz frequencies.

A new analysis approach expresses the limits of an arbitrary inverter working with ZVS in terms of allowed impedances, providing an important analytic tool for determining the limits of a certain system, evaluating load changes, control strategies, and improvement possibilities.

Driving ICP loads with resonant converters is still an open problem. This work represents a step toward the comprehension of what is feasible and to establish the way to achieve high efficient and compact power conversion in MHz range for the presented applications.

This work proposes as well a basic control strategy that would make it possible to control every variation that ICP loads exhibit. Without being compensated, these variations mean a limiting factor and destruction of such systems.

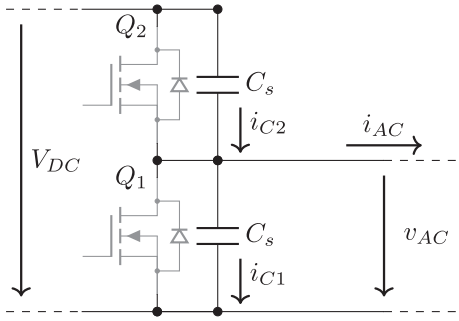

Fig. 14. Switching node with the relevant magnitudes defined.

The mentioned contributions were shown through the simplicity of a series *RLC*-circuit as resonant circuit. However, the whole analysis and approach is easily applicable to more complex resonant circuits, giving even more significance and expanding the application field of the present work.

Of particular interest for future works is the testing of a concrete high pressure system. On one hand, the ignition transient for those loads is slower than for that which is shown in this article. On the other hand, they exhibit the mentioned thermal transient and require higher ignition fields intensities. This would offer the possibility of putting under test both a frequency variation during ignition (since it would be mandatory) as well as a slow control loop that compensates the thermal processes coming afterwards.

The provided theoretical analysis for the SOA of resonant converters also provides the possibility of a serious determination of the absolute maximum power that such a converter is intrinsically able to provide at a desired frequency. To perform such calculations and verify them experimentally for the cutting-edge wide band-gap power transistors is also a highly interesting future working line.

Appendix

A. Safe Operation Area Determination

In this appendix, the mathematical background for the diagram in Fig. 3 will be exposed.

During the switching time, both transistors are blocked and the load current is just drawn by the snubber capacitors (see Fig. 14). The voltage dynamic can be obtained by relating the capacitor equations with the load current at the switching node, resulting in

$$\left.\begin{aligned} i_{C1} &= C_s \tfrac{d}{dt} v_{\mathrm{AC}} \\ i_{C2} &= C_s \tfrac{d}{dt} \left(V_{DC} - v_{\mathrm{AC}}\right) \\ i_{\mathrm{AC}} &= i_{C2} - i_{C1} \end{aligned}\right\} \Rightarrow i_{\mathrm{AC}} = -2C_s \frac{d}{dt} v_{\mathrm{AC}}. \quad (5)$$

Analyzing the switching transient when the output voltage commutates from $v_{\mathrm{AC}} = V_{DC}$ to $v_{\mathrm{AC}} = 0$, the integral of (5) provides the voltage over time

$$v_{\mathrm{AC}}(t) = -\frac{1}{2C_s} \int_{\frac{T}{2}-\frac{\tau}{2}}^{t} i_{\mathrm{AC}} dt + v_{\mathrm{AC}}(t)\Big|_{t=\frac{T}{2}-\frac{\tau}{2}} \quad (6)$$

$$= V_{DC} - \frac{1}{2C_s} \int_{\frac{T}{2}-\frac{\tau}{2}}^{t} i_{\mathrm{AC}} dt \quad (7)$$

for the time references defined in Fig. 2. In the same time frame, the current can be written as

$$i_{\mathrm{AC}}(t) = \sqrt{2} I_{\mathrm{AC}} \cos\left(\omega t + \pi + \varphi\right) \quad (8)$$

where φ is not the phase of the impedance Z_{AC} but $\varphi = \frac{\pi}{2} - \arg(Z_{\mathrm{AC}})$ as defined in Fig. 2. Substituting the expression (8) in (7), and solving the integral results in

$$v_{\mathrm{AC}}(t) = V_{DC} + \frac{I_{\mathrm{AC}}}{\sqrt{2} C_s \omega} \left(\sin\left(\omega t + \varphi\right) + \sin\left(\varphi - \pi \frac{\tau}{T}\right)\right) \quad (9)$$

which describes the output voltage *just* during the transition. Moreover, from the definition of τ as the switching time

$$v_{\mathrm{AC}}\left(\frac{T}{2} + \frac{\tau}{2}\right) = 0 \quad (10)$$

and substituting in (9), it results

$$V_{DC} + \frac{I_{\mathrm{AC}}}{\sqrt{2} C_s \omega} \left(\sin\left(\varphi - \pi \frac{\tau}{T}\right) - \sin\left(\varphi + \pi \frac{\tau}{T}\right)\right) = 0. \quad (11)$$

Under the approximation of a high enough quality factor [1], the effective current I_{AC} can be expressed in terms of the amplitude of first harmonic of the voltage. The first Fourier coefficient of a voltage waveform like the showed in Fig. 2 can be calculated[2] resulting in

$$V_{\mathrm{AC}}^{(1)} = V_{DC} \frac{\sqrt{2}}{\pi} \mathrm{sinc}\left(\frac{\tau}{T}\right) \quad (12)$$

having consequently

$$I_{\mathrm{AC}} = \frac{V_{\mathrm{AC}}^{(1)}}{|Z_{\mathrm{AC}}|} = \frac{V_{DC}}{|Z_{\mathrm{AC}}|} \frac{\sqrt{2}}{\pi} \mathrm{sinc}\left(\frac{\tau}{T}\right). \quad (13)$$

Making this substitution in (11) and using

$$\sin\left(a+b\right) - \sin\left(a-b\right) = 2\cos\left(a\right)\sin\left(b\right)$$

$$\cos\left(\varphi\right) = \frac{X_{\mathrm{AC}}}{|Z_{\mathrm{AC}}|}$$

results in

$$\frac{|Z_{\mathrm{AC}}|^2}{X_{\mathrm{AC}}} C_s f \pi = \frac{\tau}{T} \mathrm{sinc}^2\left(\frac{\tau}{T}\right) := \chi\left(\frac{\tau}{T}\right). \quad (14)$$

The function $\chi(\frac{\tau}{T})$ is plotted in Fig. 15. Its maximum has no analytical expression but a numerical approximation results in $\chi^* \approx 0.23$ at $\frac{\tau^*}{T} \approx 0.37$.

The left side of (14) can be expressed in terms of the normalized quantities

$$\begin{aligned} Z_r &:= Z_{\mathrm{AC}} f C_s \\ R_r &:= R_{\mathrm{AC}} f C_s \\ X_r &:= X_{\mathrm{AC}} f C_s \end{aligned} \quad (15)$$

[2]Under the approximation of a linear voltage transition.

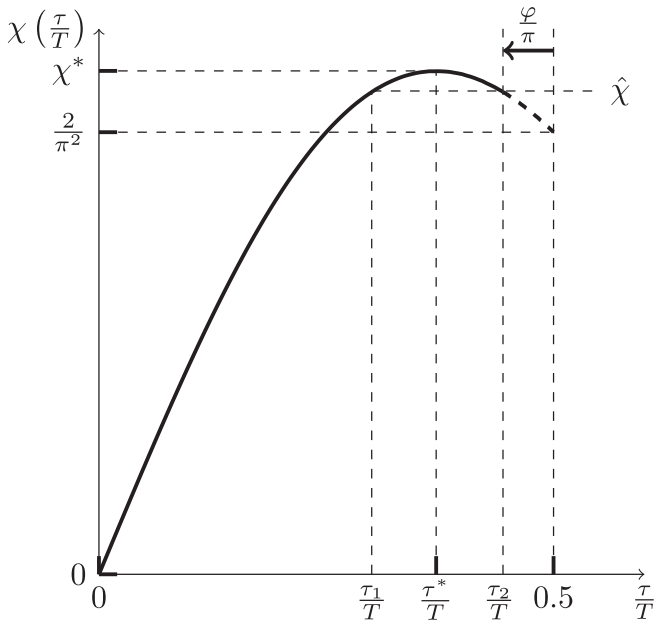

Fig. 15. Function $\chi(\frac{\tau}{T})$. Example with $\varphi = 10\,^\circ$.

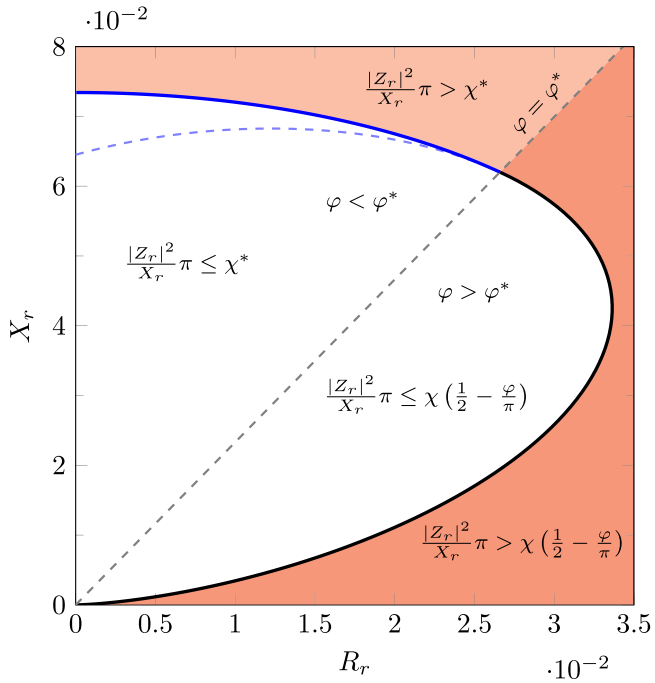

Fig. 16. Discussion of impedance regions where ZVS is achieved.

what reduces (14) to

$$\chi\left(\frac{\tau}{T}\right) = \frac{|Z_r|^2}{X_r}\pi. \tag{16}$$

From Fig. 2 it can be seen that, for the output voltage to be zero *before* the current changes its polarity it must be

$$\frac{\tau}{2} \leq \frac{T}{4} - \frac{\varphi}{\omega} \Rightarrow \frac{\tau}{T} \leq \frac{1}{2} - \frac{\varphi}{\pi} \tag{17}$$

what reduces the range of possible values for $\frac{\tau}{T}$ (arrow at right side of Fig. 15). From here on, it just need to be discussed which possible solutions (16) has, depending on the angle φ (indirectly the load phase). It will be done with help of Fig. 15, building step-by-step the diagram of Fig. 16.

In the normalized impedance plane $X_r - R_r$ (see Fig. 16), the critical angle $\varphi^* = \frac{\pi}{2} - \frac{\pi\tau^*}{T}$ is marked with the gray dashed line.

For $\varphi^* \leq \varphi \leq \pi/2$ (when the arrow of Fig. 15 passes the relative maximum), (16) can just give one solution since for $0 < \frac{\tau}{T} < \frac{\tau^*}{T}$ the function χ is monotone. In this case, ZVS will be achieved for the impedances that satisfy

$$\frac{|Z_r|^2}{X_r}\pi \leq \chi\left(\frac{1}{2} - \frac{\varphi}{\pi}\right). \tag{18}$$

The impedances that make (18) to an equality correspond to the cases where the output voltage achieves its relative minimum exactly at $v_{\mathrm{AC}} = 0$, showed in Fig. 16 by the thick black curve.

For $0 \leq \varphi < \varphi^*$, two different cases must be distinguished. The angle φ corresponds in Fig. 15 to $\frac{\tau_2}{T}$ defining the value $\hat{\chi} = \chi(\tau_2/T)$. Because of the relative maximum of the function χ, there is another value for the switching time $\tau = \tau_1$ which also corresponds to $\hat{\chi}$. This divides the analysis in the following two cases:

$$\text{(I)}: \hat{\chi} \leq \frac{|Z_r|^2}{X_r}\pi < \chi^*$$

$$\text{(II)}: 0 \leq \frac{|Z_r|^2}{X_r}\pi < \hat{\chi}.$$

For case (I), there will be always two solutions τ_A and τ_B so that

$$\chi\left(\frac{\tau_A}{T}\right) = \chi\left(\frac{\tau_B}{T}\right) = \frac{|Z_r|^2}{X_r}\pi \tag{19}$$

with $\tau_1 < \tau_A < \tau^* < \tau_B < \tau_2$. ZVS will be then lost for

$$\frac{|Z_r|^2}{X_r}\pi > \chi^*. \tag{20}$$

For the border case

$$\frac{|Z_r|^2}{X_r}\pi = \chi^* \tag{21}$$

the solution is just one $\tau = \tau_A = \tau_B = \tau^*$, determining this way the ZVS border in blue from Fig. 16.

For case (II), there will be just one solution, being

$$\frac{\tau}{T} = \chi^{-1}\left(\frac{|Z_r|^2}{X_r}\pi\right). \tag{22}$$

The border between case (I) and case (II) corresponds to the impedances that satisfy

$$\frac{|Z_r|^2}{X_r}\pi = \hat{\chi} \tag{23}$$

shown with a dashed sky-blue line in Fig. 16.

In summary, ZVS is achieved in all white regions from Fig. 16, having in all cases the solution

$$\frac{\tau}{T} = \min\left\{\chi^{-1}\left(\frac{|Z_r|^2}{X_r}\pi\right)\right\}. \tag{24}$$

For the region between the blue line and the sky-blue dashed line, there is a second solution

$$\frac{\tau}{T} = \max\left\{\chi^{-1}\left(\frac{|Z_r|^2}{X_r}\pi\right)\right\}. \tag{25}$$

However, this solution can be normally ignored because it represents a case which is difficult to implement. The corresponding times where the gate signal must be active are extremely short, being not practicable for the application frequencies. Furthermore, this impedance region is not of special interest because the low power that can be transferred there.

Finally, in the region where ZVS is achieved, not only the voltage waveform is determined (since $\frac{\tau}{T}$ is determined) but also the normalized current, and power

$$I_r := \frac{I_{\mathrm{AC}}}{V_{DC} f C_s}$$

$$P_r := \frac{P}{V_{DC}^2 f C_s}$$

which makes this diagram especially useful for the design stage with variable loads. In Fig. 3, contour lines for τ/T, I_r, and P_r are shown.

When using the presented diagram for designing a concrete system, practical limitations must be added, reducing the ZVS region to the actual allowed region. The lines where τ/T are constant can be used for example for determining the region where dV/dt is under certain desired limit, as for avoiding EMI issues. Analogously, current limits of the used devices and timing uncertainties from the driving system can be traduced in extra constraints in the diagram. With such a procedure, the absolute maximum power that can be delivered by a certain inverter, at a desired frequency and with a certain snubber capacitance can be determined, as well as the needed output impedance that makes this possible.

B. Output Waveforms During the Transient

Figs. 17– 20 show the inverter output current i_{AC} and output voltage v_{AC} at four different times during the ignition transient, showing that ZVS is kept. The time reference is the same used in Section V-B1. Fig. 17 corresponds to OFF-state at $t = 0\,\mathrm{ms}$, whereas Fig. 20 to a completely expanded plasma at $t = 0.3\,\mathrm{ms}$. The voltage and current amplitude are slightly lower as the showed in Section V-B1, which corresponds to exactly the same setup but to a different measurements run. This small difference can be explained through the strong dependence of the needed magnetic field for ignition on story of the lamp. This effect is due to the ion trapping in the quartz lamp body, also known as long therm charge memory effect, which is treated in [47] and [48], and is out of the scope of the present work.

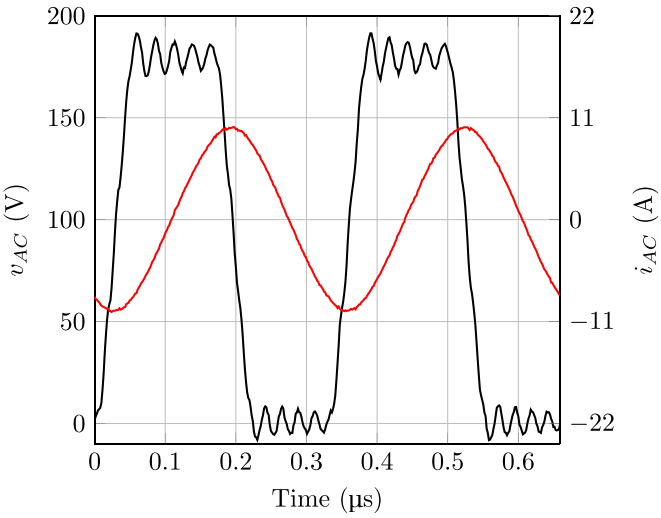

Fig. 17. Inverter output current (red), and voltage (black) at $t = 0\,\mathrm{ms}$.

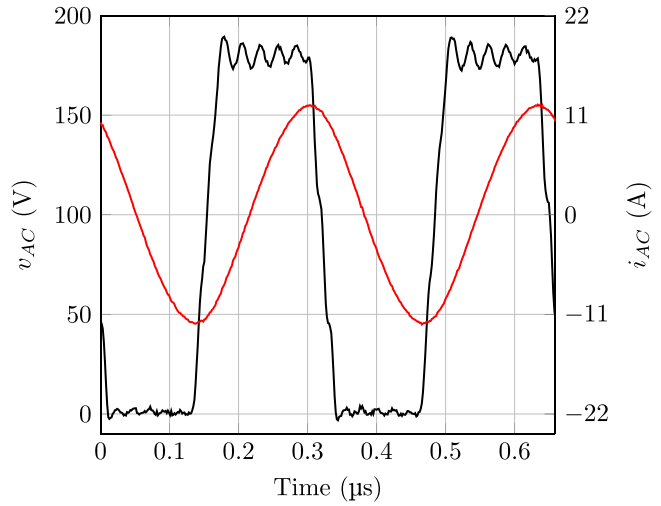

Fig. 18. Inverter output current (red), and voltage (black) at $t = 0.1\,\mathrm{ms}$.

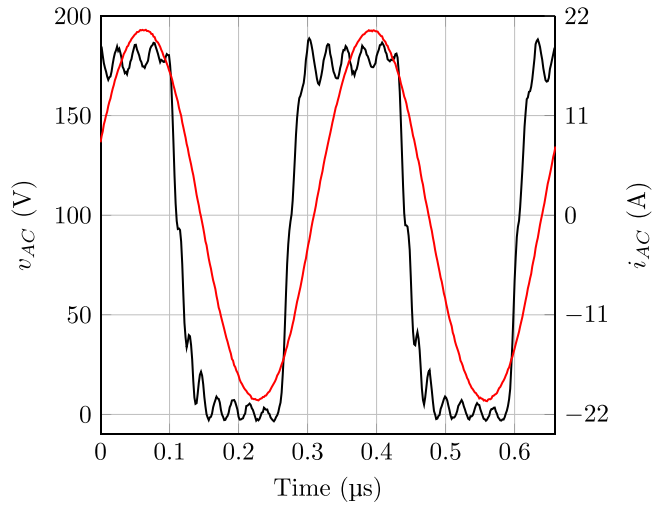

Fig. 19. Inverter output current (red), and voltage (black) at $t = 0.2\,\mathrm{ms}$.

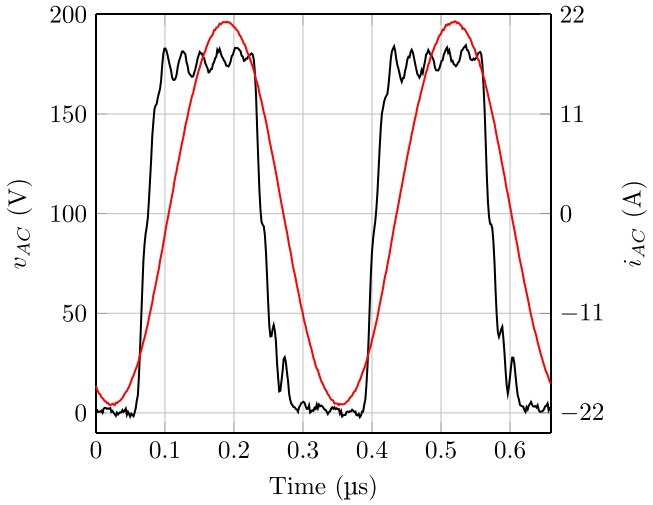

Fig. 20. Inverter output current (red), and voltage (black) at $t = 0.3\,\text{ms}$.

REFERENCES

[1] M. Kazimierczuk and D. Czarkowski, *Resonant Power Converters*. Hoboken, NJ, USA: Wiley, 1995.

[2] *Inductive Discharges*. Hoboken, NJ, USA: Wiley, 2005, ch. 12, pp. 461–489. [Online]. Available: https://onlinelibrary.wiley.com/doi/abs/10.1002/0471724254.ch12

[3] M. Mehdizadeh, "Chapter 10 - plasma applicators at RF and microwave frequencies," in *Proc. Microw./RF Applicators Probes*, 2015, pp. 335–363. [Online]. Available: https://www.sciencedirect.com/science/article/pii/B9780323322560000105

[4] R. Bolot, C. Coddet, C. Schreuders, M. Leparoux, and S. Siegmann, "Modeling of an inductively coupled plasma for the synthesis of nanoparticles," *J. Thermal Spray Technol.*, vol. 16, pp. 690–697, 2007.

[5] T. Gehring, F. Denk, Q. Jin, S. Eizaguirre, and R. Kling, "Inductive medium pressure UV-source," *Plasma*, vol. 3, no. 1, pp. 1–9, 2020.

[6] M. SuprabhaK. PandeJ. DixitDiwan, and C. P. Kaushik, "Design of 50 kW, 5 MHz RF plasma power supply for low and intermediate level radioactive waste management," in *Proc. IEEE 1st Int. Conf. Power Electron., Intell. Control Energy Syst.*, 2016, pp. 1–3.

[7] R. Bolot, C. Coddet, C. Schreuders, M. Leparoux, and S. Siegmann, "Modeling of an inductively coupled plasma for the synthesis of nanoparticles," *J. Thermal Spray Technol.*, vol. 16, pp. 690–697, 2007.

[8] B. Patil, Q. Wang, V. Hessel, and J. Lang, "Plasma n2-fixation: 1900-2014," *Catalysis Today*, vol. 256, pp. 49–66, 2015. [Online]. Available: http://www.sciencedirect.com/science/article/pii/S0920586115002989

[9] M. Ben Yaala *et al.*, "Plasma-assisted catalytic formation of ammonia in N2-H2 plasma on a tungsten surface," *Phys. Chem. Chem. Phys.*, vol. 21, pp. 16623–16633, 2019. [Online]. Available: http://dx.doi.org/10.1039/C9CP01139 K

[10] F. Denk, "Design und entwicklung von MHz-Wechselrichtern für den leistungsbereich über 10 kW," Ph.D. dissertation, Lichttechnisches Institut, Karlsruher Insitut für Technologie, Karlsruhe, Germany, 2019.

[11] A. Eroglu, *Linear and Switch-Mode RF Power Amplifiers: Design and Implementation Methods*. Boca Raton, FL, USA: CRC Press, 2018. [Online]. Available: https://search.ebscohost.com/login.aspx?direct=true&scope=site&db=nlebk&db=nlabk&AN=1590431

[12] G. Meneghesso, *Gallium Nitride-Enabled High Frequency and High Efficiency Power Conversion (Integrated Circuits and Systems Series)*. Cham, Switzerland: Springer, 2018. [Online]. Available: https://ebookcentral.proquest.com/lib/kxp/detail.action?docID=5394420

[13] M. Kazimierczuk, *RF Power Amplifiers*, 2nd ed. Chichester, U.K.: Wiley, 2015. [Online]. Available: https://search.ebscohost.com/login.aspx?direct=true&scope=site&db=nlebk&db=nlabk&AN=870148

[14] N. K. Trung and K. Akatsu, "Design high power and high efficiency inverter operating at 13.56 Mhz for wireless power transfer systems," in *Proc. IEEE Energy Convers. Congr. Expo.*, 2016, pp. 1–8.

[15] J. T. Gudmundsson and M. A. Lieberman, "Magnetic induction and plasma impedance in a cylindrical inductive discharge," *Plasma Sources Sci. Technol.*, vol. 6, no. 4, pp. 540–550, Nov. 1997. [Online]. Available: https://doi.org/10.1088/0963-0252/6/4/012

[16] J. Fouladgar and A. Chentouf, "The calculation of the impedance of an induction plasma installation by a hybrid finite-element boundary-element method," *IEEE Trans. Magn.*, vol. 29, no. 6, pp. 2479–2481, Nov. 1993.

[17] D. Bernardi, V. Colombo, G. G. M. Coppa, and A. D'Angola, "Simulation of the ignition transient in RF inductively-coupled plasma torches," *Euro. Phys. J. D. - Atomic, Mol., Opt. Plasma Phys.*, vol. 14, no. 3, pp. 337–348, Jun. 2001. [Online]. Available: https://doi.org/10.1007/s100530170201

[18] J. Fouladgar and A. Chentouf, "The calculation of the impedance of an induction plasma installation by a hybrid finite-element boundary-element method," *IEEE Trans. Magn.*, vol. 29, no. 6, pp. 2479–2481, Nov. 1993.

[19] M. A. Razzak, K. Kondo, Y. Uesugi, N. Ohno, and S. Takamura, "Transition from electrostatic-to-electromagnetic mode in a radio-frequency ar inductively coupled plasma in atmospheric pressure," *J. Appl. Phys.*, vol. 95, no. 2, pp. 427–433, 2004. [Online]. Available: https://doi.org/10.1063/1.1635650

[20] X. Zhang, P.-C. Yu, Y. Liu, Z. Zheng, L. Xu, P. Wang, and J.-X. Cao, "The transition mechanisms of the E to H mode and the H to E mode in an inductively coupled argon-mercury mixture discharge," *Phys. Plasmas*, vol. 22, no. 10, 2015, Art. no. 103509. [Online]. Available: https://doi.org/10.1063/1.4933035

[21] J.-K. Lee, H.-C. Lee, and C.-W. Chung, "E-H mode transition in inductively coupled plasma using Ar, O_2, N_2, and mixture gas," *Current Appl. Phys.*, vol. 11, no. 5, pp. S149–S153, 2010. [Online]. Available: https://www.sciencedirect.com/science/article/pii/S1567173911002203

[22] M. M. Turner and M. A. Lieberman, "Hysteresis and the E-to-H transition in radiofrequency inductive discharges," *Plasma Sources Sci. Technol.*, vol. 8, no. 2, pp. 313–324, Jan. 1999. [Online]. Available: https://doi.org/10.1088/0963-0252/8/2/312

[23] U. Kortshagen, N. D. Gibson, and J. E. Lawler, "On the E - H mode transition in RF inductive discharges," *J. Phys. D: Appl. Phys.*, vol. 29, no. 5, pp. 1224–1236, May 1996. [Online]. Available: https://doi.org/10.1088/0022-3727/29/5/017

[24] Y. Han, O. Leitermann, D. A. Jackson, J. M. Rivas, and D. J. Perreault, "Resistance compression networks for radio-frequency power conversion," *IEEE Trans. Power Electron.*, vol. 22, no. 1, pp. 41–53, Jan. 2007.

[25] A. Al Bastami *et al.*, "Dynamic matching system for radio-frequency plasma generation," *IEEE Trans. Power Electron.*, vol. 33, no. 3, pp. 1940–1951, Mar. 2018.

[26] C. Bowick, J. Blyler, and C. Ajluni, "Chapter 4 - impedance matching," in *Proc. RF Circuit Des.*, 2008, pp. 63–102. [Online]. Available: https://www.sciencedirect.com/science/article/pii/B9780750685184500060

[27] COMSOL multiphysics v.55. www.comsol.com. COMSOL AB, Stockholm, Sweden, 2019. [Online]. Available: www.comsol.com

[28] *Comsol PlasmaModule User's Guide*, COMSOL AB, Stockholm, Sweden, 2015.

[29] T. J. Sommerer, "Model of a weakly ionized, low-pressure xenon dc positive column discharge plasma," *J. Phys. D: Appl. Phys.*, vol. 29, no. 3, pp. 769–778, 1996.

[30] "Hayashi database," 2020. [Online]. Available: www.lxcat.net.

[31] Biagi-v7.1 (Magboltz version 7.1), 2020. [Online]. Available: www.lxcat.net

[32] S. F. Biagi, *MagBoltz*. 2020. [Online]. Available: www.lxcat.net.

[33] A. Kramida and Y. Ralchenko, *NIST Atomic Spectra Database, NIST Standard Reference Database 78*, National Institute of Standards and Technology, Gaithersburg, MD, USA 1999.

[34] "TRINITI database," 2020. [Online]. Available: www.lxcat.net

[35] "SIGLO database," 2020. [Online]. Available: www.lxcat.net

[36] F. Denk *et al.*, "25 kW high power resonant inverter operating at 2.5 MHz based on SiC SMD phase-leg modules," in *Proc. PCIM Europe: Int. Exhib. Conf. Power Electron., Intell. Motion, Renewable Energy Manage.*, 2018, pp. 714–720.

[37] EA-PS 9000 3 U 3.3, *Kw-15 Kw-Datasheet*, EA Elektro-Automatik GmbH & Co. KG, Viersen, Germany.

[38] *MSO Serie 5 MSO54 MSO56 MSO58-Datasheet*, Tektronix, Inc., Beaverton, OR, USA 2018.

[39] *Pearson Current Monitor Model 6600 - Datasheet*, Pearson Electronics, Palo Alto, CA, USA, 2004.

[40] *30 A. AC/DC Current Probe-TCP0030 A Datasheet*, Tektronix, Inc., Beaverton, OR, USA 2017.

[41] PMK Mess- und Kommunikationstechnik GmbH, Bad Soden, Germany, 2020.

[42] DET10A(/M) - *Si Biased Detector - Datasheet*, Thorlabs Inc., Newton, NJ, USA, 2017.

[43] J. C. Camparo and C. M. Klimcak, "Generation of ion-acoustic waves in an inductively coupled, low-pressure discharge lamp," *J. Appl. Phys.*, vol. 99, no. 8, 2006, Art. no. 83306. [Online]. Available: https://doi.org/10.1063/

[44] J. C. Camparo and R. Mackay, "Ion-wave stabilization of an inductively coupled plasma," *Appl. Phys. Lett.*, vol. 88, no. 17, 2006, Art. no. 173510. [Online]. Available: https://doi.org/10.1063/1.2198108
[45] A. Kramida, Y. Ralchenko, J. Reader, and NIST ASD Team, "NIST atomic spectra database (ver. 5.8)," 2020. [Online]. Available: https://physics.nist.gov/asd
[46] D. Han and B. Sarlioglu, "Deadtime effect on GAN-based synchronous boost converter and analytical model for optimal deadtime selection," *IEEE Trans. Power Electron.*, vol. 31, no. 1, pp. 601–612, Jan. 2016.
[47] P. F. Ambrico, M. Ambrico, L. Schiavulli, and S. D. Benedictis"2D thermoluminescence imaging of dielectric surface long term charge memory of plasma surface interaction in DBD discharges," *J. Phys. D: Appl. Phys.*, vol. 47, no. 30, Jul. 2014, Art. no. 305201. [Online]. Available: https://doi.org/10.1088/0022-3727/47/30/305201
[48] M. Li, C. Li, H. Zhan, J. Xu, and X. Wang, "Effect of surface charge trapping on dielectric barrier discharge," *Appl. Phys. Lett.*, vol. 92, no. 3, 2008, Art. no. 031503.

Santiago Eizaguirre Cabrera received the Ing. degree in electrical engineering from the University of the Republic, Montevideo, Uruguay, in 2017.

Since 2017, he has been a Researcher on his doctoral thesis with the Light Technology Institute, Karlsruhe Institute of Technology, Karlsruhe, Germany. His research interests include the use of wide band-gap power transistors for the high efficient, high power conversion in MHz range with resonant converters for plasma generation applications.

Tim Gehring studied micro- and nanotechnology from the Kaiserslautern University of Applied Sciences, Kaiserslautern, Germany, and recieved the M.Eng. degree in 2016 from the same university.

Since 2016, he has been a Research Assistant with the Light Technology Institute, Karlsruhe Institute of Technology, Karlsruhe, Germany. His research interests include plasma technology for ICP radiation sources and ICP atmospheric pressure plasmas, such as plasma torches.

Jan Dycke was born in 1993. He received the bachelor's degree in 2019 and the master's degree in electrical engineering and information technology from the Karlsruhe Institute of Technology, Karlsruhe, Germany, in 2021.

He is currently a Researcher with the Light Technology Institute, Karlsruhe Institute of Technology. His research interests include resonant converters operating in the MHz range and their control for plasma applications.

Qihao Jin received the bachelor's degree in optical information and technology from the Hefei University of Technology, Hefei, China, in 2013, and the master's degree in optics and photonics from the Karlsruhe Institute of Technology (KIT), Karlsruhe, Germany, in 2016.

He is currently a Scientific Researcher with KIT, focusing on tunable optical response in optoelectronics. His major research interests include understanding the mechanisms of tunable plasmons and photonic crystals via plasma-assisted nanostructuring and also exploring the use of micro/nanoscale printing technology to build optical and biological sensors.

Fabian Denk received the master's and Ph.D. degrees in electrical engineering from the Karlsruhe Institute of Technology (KIT), Karlsruhe, Germany, in 2014 and 2019, respectively.

For his doctoral thesis, he worked as a Researcher on high power MHz inverters with the Light Technology Institute, KIT.

Manuel Renschler was born in 1993. He received the B.Eng. and master's degrees in sensor technology from the Karlsruhe University of Applied Sciences, Karlsruhe, Germany, in 2018 and 2021, respectively.

He did his master's thesis with the Light Technology Institute, Karlsruhe Institute of Technology, Karlsruhe, Germany, developing ICP simulations based on real systems.

Marc Hiller (Member, IEEE) received the diploma degree from the Technische Universität Darmstadt, Darmstadt, Germany, in 1993, and the Ph.D. degree from the Universität der Bundeswehr München, Neubiberg, Germany, in 2008, both in electrical engineering.

Since 2005, he has been with the Drive Technology Division, Sector Industry, Siemens AG, Nuremberg, Germany, where he was the Project Manager in the development of industrial medium-voltage drives. His research interests include modern power-hardware-in-the-loop converters, modeling of electrical drives and grids, and grid connected converter, energy storage integration, and the control of power semiconductors.

Dr. Hiller has been the Chair of Power Electronic Systems with the Karlsruhe Institute of Technology, Karlsruhe, Germany, since 2015.

Uli Lemmer (Member, IEEE) received the diploma degree in physics from RWTH Aachen University, Aachen, Germany, in 1990, and the Ph.D. degree from the University of Marburg, Marburg, Germany, in 1995.

From 1995 to 1996, he held a Postdoctoral Position with the University of California at Santa Barbara, Santa Barbara, CA, USA. From 1996 to 2002, he was with the University of Munich, Munich, Germany. In 2002, he was appointed as a Full Professor and the Director of the Light Technology Institute, Karlsruhe Institute of Technology, Karlsruhe, Germany. Since 2006, he has also been the Coordinator of the Karlsruhe School of Optics and Photonics, Karlsruhe, Germany, and he is also heading the device physics competence center within the InnovationLab, Heidelberg, Germany. His research interests include technology and the applications of printable organic and inorganic semiconductors.

Rainer Kling (Member, IEEE) received the Dipl.Ing. degree in optical information technology and the Ph.D. degree in pulsed excimer lamps from the University of Karlsruhe, Karlsruhe, Germany, in 1991 and 1997, respectively.

From 1998 to 2008, he was with Osram GmbH, Munich, Germany, as R&D Head and BU Head. Since 2008, he has been an Associate Professor with Light Technologies Institute, Karlsruhe Institute of Technology, Karlsruhe, Germany. He has authored or coauthored 140 publications and 29 intellectual properties in the fields of lamps and plasma physics. His research interests include radiation sources and wide band gap electronic ballasts.

Dr. Kling is the Vice President of the German Academy of Photobiology and Phototechnology (DAfP) and a Board Member of the German Light Technology Society (LITG). He is a member of German Physical Society.